AIP | Journal of Applied Physics

Trapped hybrid modes in solidly mounted resonators based on c-axis oriented hexagonal crystals

Adam D. Wathen, Farasat Munir, and William D. Hunt

Citation: J. Appl. Phys. **108**, 114503 (2010); doi: 10.1063/1.3517097

View online: http://dx.doi.org/10.1063/1.3517097

View Table of Contents: http://jap.aip.org/resource/1/JAPIAU/v108/i11

Published by the American Institute of Physics.

Trapped hybrid modes in solidly mounted resonators based on c-axis oriented hexagonal crystals

Adam D. Wathen, Farasat Munir, and William D. Hunt[a)]
School of Electrical and Computer Engineering, Georgia Institute of Technology, 791 Atlantic Dr., Atlanta, Georgia 30332, USA

(Received 17 September 2010; accepted 17 October 2010; published online 6 December 2010)

Assuming an idealized piezoelectric bulk acoustic wave resonator, one typically calculates the velocity of the fundamental bulk acoustic mode as the measured frequency times twice the thickness of the piezoelectric film. In c-axis 6*mm* hexagonal crystals of (e.g., ZnO or AlN), both the longitudinal and thickness shear modes are peizoelectrically active using thickness excitation and lateral-field excitation, respectively. Without a loss of generality, we concentrate our study on ZnO films. The theoretical velocity of the pure thickness shear mode in sputtered ZnO, based strictly on reported material properties, is calculated to be approximately 2580 m/s. However, a variety of acoustic velocities for the thickness shear mode in ZnO have been reported in the literature ranging from about 3100–3500 m/s. These reported values represent a 20%–36% increase in acoustic velocity relative to the theoretical values. In the literature, this deviation is typically attributed to ZnO film inconsistencies and other phenomena which can be difficult to quantify. We propose that the reported inconsistencies may be attributed to a *hybrid* acoustic mode comprised of a coupling of shear and longitudinal particle displacements. In this paper, we present a theoretical description of a hybrid mode in ZnO solidly mounted resonator (SMR) devices. We begin first with an experimental verification of a mode with a changing velocity in a ZnO SMR with the only variable being the ZnO thickness. Using the acoustic velocity through the thickness as an *effective* velocity with which to reference the mode, we find the effective acoustic velocity to range from 3100–3900 m/s, with increasing ZnO thickness. We then start from the first principles of piezoelectric acoustic wave propagation and derive three coupled partial differential equations describing a hybrid mode comprised of the coupling between longitudinal and shear particle displacement and the corresponding piezoelectrically generated potential in the ZnO film. The qualitative findings described by the derived equations are then further investigated with finite element simulation (COMSOL MULTIPHYSICS®). We simulate the performance of our experimental devices using the COMSOL platform, examine the eigenfrequencies of the structure, and find a hybrid mode which is trapped both vertically and laterally in the ZnO film. Calculating the effective velocity of the simulated modes, we find the simulated effective velocities to be within 1.5% of our measured results. Finally, we compare simulation results to experimentally measured results of a previously observed hybrid mode and achieve a 0.2% agreement. © *2010 American Institute of Physics*. [doi:10.1063/1.3517097]

I. INTRODUCTION AND BACKGROUND

In 6*mm* hexagonal crystals such as AlN and ZnO, the excitation of the longitudinal mode requires an electrical excitation *parallel* to the c-axis of the crystal[1,2] (thickness-excitation), while the excitation of the thickness-shear mode (TSM) requires an excitation *orthogonal* to the c-axis[3–5] [lateral-field excitation (LFE)]. While commonly used in filter applications, acoustic resonators have also frequently been used in sensing applications beginning with the quartz crystal microbalance[6] in 1959. The frequency of the resonator is inversely proportional to the thickness of the device and the mass sensitivity is proportional to a power of the unperturbed resonant frequency.[6–8] Thus, thinner piezoelectric films are required for higher mass sensitivity applications, resulting in concerns about device fragility as resonant frequencies enter the gigahertz (GHz) range. A solidly mounted resonator (SMR) incorporating an acoustic reflector[9] eliminates this concern and allows for the deposition of extremely thin piezoelectric films to obtain frequencies well into the GHz range. For liquid-phase sensing applications, the TSM is required in the device. In contrast to the longitudinal mode, an ideal liquid sample theoretically cannot support a shear mode. Therefore, less TSM acoustic energy propagates into the liquid, resulting in minimal degradation of device Q and, thus, better frequency resolution. Thin film TSM resonators are, therefore, highly desired in liquid-phase sensing applications.

There has been significant recent work on the excitation of the TSM in hexagonal crystals using a variety of methods. Without a loss of generality, we will restrict our discussion to ZnO, which has a hexagonal crystal structure and a long history in piezoelectric devices.[10] As an example, Wang and Lakin[11] fabricated membrane devices with the ZnO c-axis titled 40° to the surface normal. This configuration incorpo-

[a)]Electronic mail: bill.hunt@ece.gatech.edu.

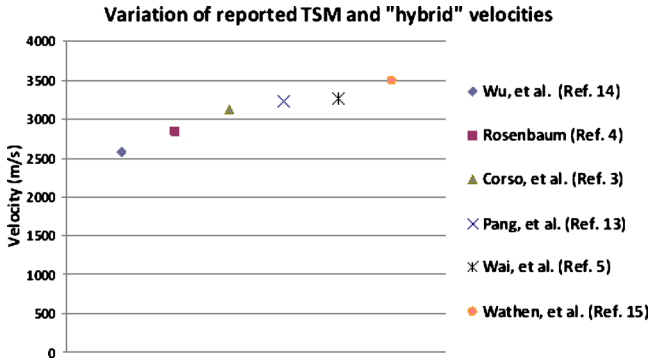

FIG. 1. (Color online) Variation in reported TSM and "hybrid" velocities.

rates an excitation electric field at an angle to the c-axis and results in the interesting consequence of exciting both the TSM and the longitudinal modes. However, these devices require sophisticated deposition and etching processes and the membrane structure is inherently fragile when dealing in the GHz range due to the extremely thin film necessary. Link *et al.*,[12] incorporated the tilted ZnO into a SMR design,[9] eliminating the aforementioned problem of fragility. However, the tilted ZnO still requires a nonstandard modification to traditional fabrication techniques. In an attempt to make the excitation field more purely lateral through the c-axis, Pang *et al.*,[13] used a lift-off technique for self-aligned c-axis ZnO to incorporate direct lateral field excitation (LFE) of the TSM. This eliminates the need for titled ZnO, and while these devices were solidly mounted, they did not incorporate an acoustic reflector and suffered from low Q. Corso *et al.*,[3] showed the excitation of the TSM in highly c-axis-oriented ZnO on a fabricated acoustic reflector stack using only a single mask step for top-layer excitation electrodes. These devices eliminated the need for any elaborate deposition or lift-off techniques and are attractive due to their fabrication simplicity.

A common way of verifying the existence of the TSM is to calculate the acoustic velocity of the mode from the measured resonant frequency and the device thickness. Assuming an ideal air-backed resonator (or air on top with a perfect acoustic reflector on the bottom), the velocity is simply calculated as $v = f_0 \times 2d$, with d being the thickness of the device. Using bulk ZnO material properties in Rosenbaum,[4] the calculated piezoelectrically stiffened TSM velocity in ZnO is 2841 m/s. Wu *et al.*, calculated the TSM velocities to be 2577 m/s and 2733 m/s for sputtered and epitaxial ZnO, respectively.[14] These velocities are theoretical calculations to which we can compare measured velocities to verify the TSM. Accounting for difference in ZnO material properties, deposition processes, parameters, and techniques, TSM velocities calculated from measurement should be within a few percent of these theoretical values. Figure 1 shows a plot of the range of calculated mode velocities in ZnO devices.[3–5,13–15] The reported values of the TSM velocity range from 2830–3368 m/s. Using the same device structure as Corso *et al.*,[3] Wathen *et al.*,[15] observed a mode with a velocity of 3500 m/s and a Q of nearly 34 000. With this velocity being nearly 1000 m/s off from the quoted sputtered ZnO TSM velocity, this mode was deemed a *hybrid* mode and is thus not considered a pure TSM. The values in Fig. 1 are all measured on devices employing sputtered ZnO. Using the sputtered ZnO TSM velocity (2580 m/s) (Ref. 14) as a baseline, these values show a 20%–36% deviation from the theoretical value. Even considering inherent differences in deposition parameters and ZnO crystallinity, it is difficult to attribute this amount of measured variance to an observed *pure* TSM.

It should be noted that only the *ideal* cases of thickness-excitation and LFE generate the *pure* longitudinal and thickness shear modes, respectively. Thickness-excitation requires a piezoelectric film sandwiched between two electrodes to provide for an electric field parallel to the c-axis. LFE requires electrodes to be on the sides of the film to provide a field orthogonal to the c-axis. In idealized models, these two configurations ignore fringing fields at the edges of the electrodes.[4] In real devices, however, these fringing fields are unavoidable, resulting in a far more complex excitation field than in the ideal case. In addition to the desired pure mode, this impure field has the capability to excite a variety of acoustic modes, which may result in a far more complex resonant mode structure than the pure mode. This resulting mode structure may be considered a *hybrid* mode.

In this paper, we present an experimental verification and a theoretical description of a hybrid acoustic mode presumably due to impure electrical excitation. We begin first with experimental observations of a resonant acoustic mode in two different electrode configurations on a ZnO SMR with an *effective* velocity that varies with ZnO thickness. A derivation of three governing partial differential equations that describe the coupling of longitudinal and shear particle displacement and the resulting piezoelectrically generated potential is then presented as a potential explanation for the hybrid mode. Finite element simulations of the two experimental SMR device configurations are presented and an eigenmode analysis confirms the existence of a resonant coupled mode trapped in the ZnO film. The simulation results are then compared to those in the experimentally measured devices. The experimental data is shown to agree with the simulated data within 1.5%.

II. EXPERIMENTAL INVESTIGATIONS

The devices used in the studies shown in Fig. 1 have a variety of electrode configurations, ZnO thicknesses, and, if employed, reflector layer thicknesses. For simplicity, we wish to reduce the variability in our study to only two independent variables, i.e., the electrode configuration and the ZnO thickness. Each of two electrode configurations will be analyzed individually, so the experiment reduces further to two separate experiments, each depending only on the ZnO thickness. The goal of this section is to determine how the resonant frequencies and *effective* acoustic velocities vary with ZnO thickness.

Beginning with the method outlined in Corso *et al.*,[3] we fabricated our own devices using the two well-defined electrode configurations shown schematically in Fig. 2. The configurations were chosen specifically to excite the TSM in the devices using LFE. The acoustic reflector stack and ZnO

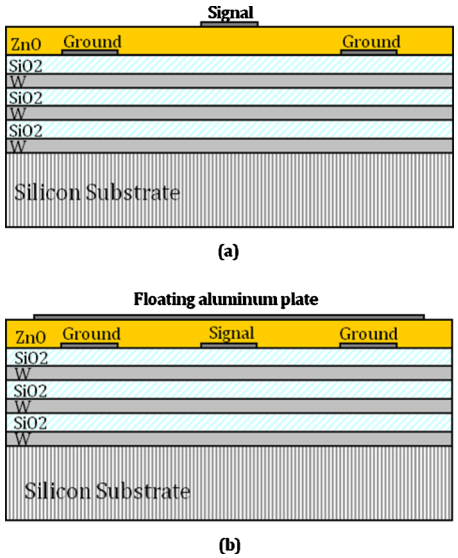

FIG. 2. (Color online) (a) Staggered electrode configuration and (b) buried electrode configuration with a floating top plate.

layer shown in Fig. 2 were fabricated using a Unifilm PVD sputtering system.[3] The stack is composed of alternating W and SiO_2 layers of 640 nm and 1000 nm thicknesses, respectively. The stack is then followed by the first Al electrode layer patterned using standard photolithography lift-off procedures and a CVC e-beam evaporation system. The electrodes start with a seed layer of 30 nm of Cr on which 145 nm of Al are evaporated. The ZnO is then RF sputtered in a 3% O_2 environment. As opposed to a uniform deposition, however, we deposit a highly nonuniform ZnO layer ranging from 1434 nm at the center down to 1015 nm at the edge of the 3 in. wafer. The top electrodes are then patterned in the same manner as the bottom. The final step is to etch the ZnO away in the appropriate locations to allow for access to the buried electrodes. The etch holes are patterned onto the wafer and a wet etch of DI water:HNO_3:HCl (80:3:1) is used to remove the excess ZnO. The thicknesses of the ZnO and electrodes were all verified by a Tencor Alpha-Step Profilometer.

The one-port scattering parameters of the devices were captured on a HP 8753C Network Analyzer with a 85047A S-parameter test set. Cascade Microtech ACP40-GSG-400 probe tips were used to probe the devices. The measured resonant frequencies and effective velocities are given in Table I.

As shown in Table I, for each electrode configuration, the resonant frequency decreases expectedly with increasing ZnO thickness. However, it is also apparent that the effective acoustic velocity *increases* with increasing ZnO thickness, continually diverging from the theoretically calculated TSM velocity in sputtered ZnO (Ref. 14) of 2577 m/s.

In addition, Shockley *et al.*, showed the trapping of acoustic energy by the inertial loading of electrodes[16] resulting in a lower acoustic velocity below (or above) them. Examining the electrode configurations used in Fig. 2, we see that the wave should then only be contained in the three regions of the ZnO that are directly below the top and above the bottom electrodes. In the case of the buried electrodes,

TABLE I. Measured resonant frequencies and effective velocities.

	Measured resonant frequencies and effective velocites			
	Buried electrodes		Staggered electrodes	
ZnO (nm)	f_0 (GHz)	Velocity (m/s)	f_0 (GHz)	Velocity (m/s)
1015	1.5496	3140	1.5482	3143
1111	1.4834	3296	1.4991	3331
1211	1.4374	3481	1.4614	3540
1324	1.4016	3711	1.4322	3792
1383	1.3731	3797	1.4123	3906
1434	1.357	3891	1.3398	3843

the additional inertial loading due to the floating plate should further lower the acoustic velocity in the energy-trapping regions, thus lowering the resonant frequency for the same ZnO thickness as compared to the staggered configuration. Therefore, for any ZnO thickness, a resonant mode in the staggered configuration of Fig. 2(a) should continually have a higher effective velocity than that in the buried configuration of Fig. 2(b). As shown in Table I, this effective velocity difference is, indeed, experimentally observed in all cases except the thickest staggered electrode configuration.

III. THEORETICAL BACKGROUND

Considering prior reports and the data gathered in Sec. II, it can be concluded that the observed mode was not the pure TSM we originally desired. With an effective velocity that increases with ZnO thickness, we can assume that the observed mode must be a kind of *hybrid* mode, possibly similar to that observed by Wathen *et al.*[15] In this section, we describe the hybrid nature of the mode as a coupling between shear and longitudinal waves.

As a theoretical treatment of the hybrid modes in these devices, we will begin with the first principles of piezoelectric and acoustic phenomena as well as imposing some constraints on the desired solution set. First, we define the strain tensor and the electric field vector, as follows:

$$\bar{S} = \begin{bmatrix} S_1 \\ S_2 \\ S_3 \\ S_4 \\ S_5 \\ S_6 \end{bmatrix} = \begin{bmatrix} \dfrac{\partial u_1}{\partial x_1} \\ \dfrac{\partial u_2}{\partial x_2} \\ \dfrac{\partial u_3}{\partial x_3} \\ \dfrac{\partial u_2}{\partial x_3} + \dfrac{\partial u_3}{\partial x_2} \\ \dfrac{\partial u_1}{\partial x_3} + \dfrac{\partial u_3}{\partial x_1} \\ \dfrac{\partial u_1}{\partial x_2} + \dfrac{\partial u_2}{\partial x_1} \end{bmatrix}, \tag{1}$$

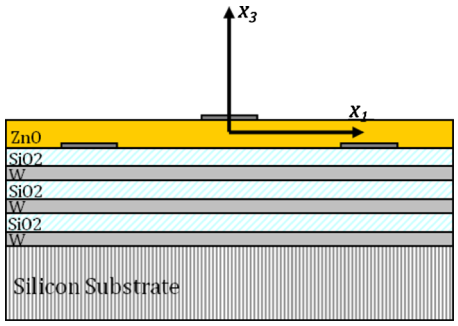

FIG. 3. (Color online) Device orientation.

$$\bar{E} = \begin{bmatrix} E_1 \\ E_2 \\ E_3 \end{bmatrix} = -\nabla\phi = -\begin{bmatrix} \frac{\partial\phi}{\partial x_1} \\ \frac{\partial\phi}{\partial x_2} \\ \frac{\partial\phi}{\partial x_3} \end{bmatrix}. \tag{2}$$

For a hexagonal crystal, like ZnO, the material tensors have the following form:

$$\bar{c}^E = \begin{bmatrix} c_{11} & c_{12} & c_{13} & 0 & 0 & 0 \\ c_{12} & c_{11} & c_{13} & 0 & 0 & 0 \\ c_{13} & c_{13} & c_{33} & 0 & 0 & 0 \\ 0 & 0 & 0 & c_{44} & 0 & 0 \\ 0 & 0 & 0 & 0 & c_{44} & 0 \\ 0 & 0 & 0 & 0 & 0 & c_{66} \end{bmatrix},$$

$$\bar{e} = \begin{bmatrix} 0 & 0 & 0 & 0 & e_{15} & 0 \\ 0 & 0 & 0 & 0 & e_{15} & 0 \\ e_{31} & e_{32} & e_{33} & 0 & 0 & 0 \end{bmatrix},$$

and

$$\bar{\varepsilon}^S = \begin{bmatrix} \varepsilon_{11} & 0 & 0 \\ 0 & \varepsilon_{11} & 0 \\ 0 & 0 & \varepsilon_{33} \end{bmatrix},$$

where $\bar{c}^E$ is the stiffness tensor at a constant electric field, $\bar{e}$ is the piezoelectric coupling tensor, and $\bar{\varepsilon}^S$ is the permittivity tensor at a constant strain. We will use the following form for the constitutive relations:

$$\bar{T} = \bar{c}^E : \bar{S} - \bar{e} \cdot \bar{E}, \tag{3a}$$

and

$$\bar{D} = \bar{\varepsilon}^S \cdot \bar{E} - \bar{e} : \bar{S}. \tag{3b}$$

For the particular configurations of the SMR devices being investigated, we search for solutions confined to a set of general restrictions for a wave propagating in the x_1-x_3-plane as illustrated in Fig. 3. Primarily, we restrict the solutions to a two-dimensional (2D) approximation with no field variations in x_2. Therefore, the desired particle polarization has components only in x_1 and x_3 directions (i.e., u_1 and u_3 are both nonzero, $u_2 = 0$) and the electric potential (Φ) also varies only in the x_1-x_3-plane.

Applying these conditions to Eqs. (1)–(3), the stress tensor and electrical displacement vector are, as follows:

$$\bar{T} = \begin{bmatrix} T_1 \\ T_2 \\ T_3 \\ T_4 \\ T_5 \\ T_6 \end{bmatrix} = \begin{bmatrix} c_{11}\frac{\partial u_1}{\partial x_1} + c_{13}\frac{\partial u_3}{\partial x_3} + e_{31}\frac{\partial\phi}{\partial x_3} \\ c_{12}\frac{\partial u_1}{\partial x_1} + c_{13}\frac{\partial u_3}{\partial x_3} + e_{31}\frac{\partial\phi}{\partial x_3} \\ c_{13}\frac{\partial u_1}{\partial x_1} + c_{33}\frac{\partial u_3}{\partial x_3} + e_{33}\frac{\partial\phi}{\partial x_3} \\ 0 \\ c_{44}\frac{\partial u_1}{\partial x_3} + c_{44}\frac{\partial u_3}{\partial x_1} + e_{15}\frac{\partial\phi}{\partial x_3} \\ 0 \end{bmatrix}, \tag{4a}$$

and

$$\bar{D} = \begin{bmatrix} -\varepsilon_{11}\frac{\partial\phi}{\partial x_1} + e_{15}\frac{\partial u_1}{\partial x_3} + e_{15}\frac{\partial u_3}{\partial x_1} \\ 0 \\ -\varepsilon_{33}\frac{\partial\phi}{\partial x_3} + e_{31}\frac{\partial u_1}{\partial x_1} + e_{33}\frac{\partial u_3}{\partial x_3} \end{bmatrix}. \tag{4b}$$

The application of Newton's Law and Gauss' Law for dielectrics to the stress and displacement tensors, respectively,

$$\nabla \cdot \bar{T} = \rho\frac{\partial^2\bar{u}}{\partial t^2}, \tag{5}$$

$$\nabla \cdot \bar{D} = 0, \tag{6}$$

and assuming time-harmonic behavior, we arrive at the following set of equations:

$$\frac{\partial T_1}{\partial x_1} + \frac{\partial T_6}{\partial x_2} + \frac{\partial T_5}{\partial x_3} = -\rho\omega^2 u_1, \tag{7a}$$

$$\frac{\partial T_6}{\partial x_1} + \frac{\partial T_2}{\partial x_2} + \frac{\partial T_4}{\partial x_3} = -\rho\omega^2 u_2, \tag{7b}$$

$$\frac{\partial T_5}{\partial x_1} + \frac{\partial T_4}{\partial x_2} + \frac{\partial T_3}{\partial x_3} = -\rho\omega^2 u_3, \tag{7c}$$

$$\frac{\partial D_1}{\partial x_1} + \frac{\partial D_3}{\partial x_3} = 0. \tag{7d}$$

Since we have assumed no particle displacement or field variations in the x_2 direction, we can eliminate the equation in u_2 and any partial derivatives with respect to x_2. Plugging Eq. (4) into Eq. (7), and grouping terms, we arrive at the following set of three coupled equations:

$$c_{11}\frac{\partial^2 u_1}{\partial x_1^2} + c_{44}\frac{\partial^2 u_1}{\partial x_3^2} + (c_{13} + c_{44})\frac{\partial^2 u_3}{\partial x_1\,\partial x_3} + (e_{31} + e_{15})\frac{\partial^2\phi}{\partial x_1\,\partial x_3} = -\rho\omega^2 u_1, \tag{8a}$$

$$c_{44}\frac{\partial^2 u_3}{\partial x_1^2} + c_{33}\frac{\partial^2 u_3}{\partial x_3^2} + (c_{13}+c_{44})\frac{\partial^2 u_1}{\partial x_1\,\partial x_3} + e_{15}\frac{\partial^2 \phi}{\partial x_1^2} + e_{33}\frac{\partial^2 \phi}{\partial x_3^2} = -\rho\omega^2 u_3, \tag{8b}$$

$$e_{15}\frac{\partial^2 u_3}{\partial x_1^2} + e_{33}\frac{\partial^2 u_3}{\partial x_3^2} + (e_{31}+e_{15})\frac{\partial^2 u_1}{\partial x_1\,\partial x_3} - \varepsilon_{11}\frac{\partial^2 \phi}{\partial x_1^2} - \varepsilon_{33}\frac{\partial^2 \phi}{\partial x_3^2} = 0. \tag{8c}$$

These equations represent the governing set of coupled PDEs for the desired set of solutions. The complexity of these equations due to the inherent coupling of u_1 and u_3 as well as the coupled dependence on Φ in the equation for u_1 in Eq. (8a) make an analytical solution to these equations difficult to obtain. But, there are several interesting qualitative features embedded in the equations that shed a bit more light on the coupling between the particle displacements.

First, let us consider that potential solutions include modes which are a superposition of LFE and thickness-excited waves. As described in Sec. I, each of these excitations theoretically produces a pure thickness-shear and longitudinal wave, respectively. Applying the restrictions appropriate for each of the pure modes, we should observe the decomposition of the coupled PDEs into the wave equations for the pure modes. For a laterally excited TSM, we require that only lateral particle displacement, i.e., u_1 components, exist. Further, for the ideal case, all variation in particle displacement in x_1 is eliminated, i.e., $\partial/\partial x_1 = 0$. Also, in LFE devices, a traveling piezoelectrically generated potential does not exist.[4] Therefore, terms in u_3, terms involving the electric potential, and any terms with second partial derivatives with respect to both x_1 and x_3 are all zero. Under these ideal conditions, the only remaining equation is

$$c_{44}\frac{\partial^2 u_1}{\partial x_3^2} = -\rho\omega^2 u_1, \tag{9}$$

which is the fundamental wave equation for a propagating TSM in a c-axis oriented hexagonal crystal.

We now wish to see if the equations decompose into the pure longitudinal mode in ZnO. In this case, we will restrict the conditions to waves with particle displacement in u_3 only and with field variation in the x_3-direction. Therefore, all mixed partial derivatives are again zero. In contrast to LFE devices, an internal potential does exist in thickness excitation, and is in the direction of the excitation itself.[4] Therefore, the potential is allowed to vary only in x_3. Equation (8c) thus reduces to

$$e_{33}\frac{\partial^2 u_3}{\partial x_3^2} = \varepsilon_{33}\frac{\partial^2 \phi}{\partial x_3^2}. \tag{10}$$

We plug this into Eq. (8b) and arrive at the fundamental wave equation for the longitudinal mode, as follows:

$$\left(c_{33} + \frac{e_{33}^2}{\varepsilon_{33}}\right)\frac{\partial^2 u_3}{\partial x_3^2} = -\rho\omega^2 u_3. \tag{11}$$

The decomposition of the coupled PDEs into the solutions for the pure TSM and longitudinal modes provides verification that the derived equations are, in fact, describing the coupling between longitudinal and shear particle displacements that reduce to the pure modes provided we apply the appropriate restrictions.

IV. FINITE ELEMENT SIMULATION

Given the complexity of the governing equations derived above, we now use a finite element simulation package, specifically COMSOL MULTIPHYSICS®, to gain further insight on the potential solutions of Eq. (8). Using the MEMS multiphysics module of COMSOL, we can simulate the piezoelectric generation of acoustic waves and examine resulting particle displacements, potentials, etc. In this section, we simulate SMR device response by employing the eigenfrequency simulation in COMSOL to determine the eigenmodes of our experimental structures used in Sec. II (Fig. 2).

We use the default ZnO stiffness, permittivity, and piezoelectric coupling tensors in COMSOL as the material parameters.[17] We first define the materials in each subdomain of the simulation (i.e., W, SiO_2, Si, and c-axis ZnO). Next, the mechanical boundary conditions of every boundary are defined as free-moving boundaries. Referring to Fig. 2, the boundaries of the electrodes defined as "ground" were set to *ground* in the simulation. The "signal" electrodes were set to *floating* ($\hat{n}\cdot\vec{D}_2=\rho_s$) as this allows for the eigenfrequencies of the solutions to correspond directly to the frequency of the applied electrical excitation. In the experimental devices, the electrical excitation occurs only at the ground and signal electrodes. No other boundaries are physically connected to either the ground or the signal paths. Therefore, all other metal boundaries must be regarded as having floating potentials as well. To accommodate this effect, we set all tungsten boundaries and the floating plate to a *floating* condition. All remaining boundaries were set to electrical *continuity* [i.e., $\hat{n}\cdot(\vec{D}_2-\vec{D}_1)=0$].

Dimensionally, the simulated structures are identical to our experimental structures presented in Sec. II. The W layers are 640 nm, the SiO_2 layers are 1000 nm, the electrodes are 175 nm thick and 40 μm wide, and the lateral gap between the electrodes is 20 μm. The overall structure is 200 μm wide and the floating plate in Fig. 2(b) is 180 μm wide. The initial ZnO thickness is 1015 nm. Later, we increase the ZnO thickness to match the experimental thickness shown in Table I and observe the resulting eigenmodes.

Considering the conditions prescribed in Sec. III, we desire a mode with energy mostly contained within in the ZnO layer and propagates only in the x_1-x_3-plane. Further, due to the energy trapping considerations described in Sec. II,[16] the mode should also be trapped laterally within the confines of the electrodes. Due to structural imperfections and the physical necessity for finite Q, some energy leakage outside of these regions is expected and will be present in all satisfactory solutions. For a ZnO thickness of 1015 nm, the mode profiles that satisfy these criteria are shown in Figs. 4 and 5.

Since these are the only simulated modes present in the structure that satisfy our criteria described above, we now

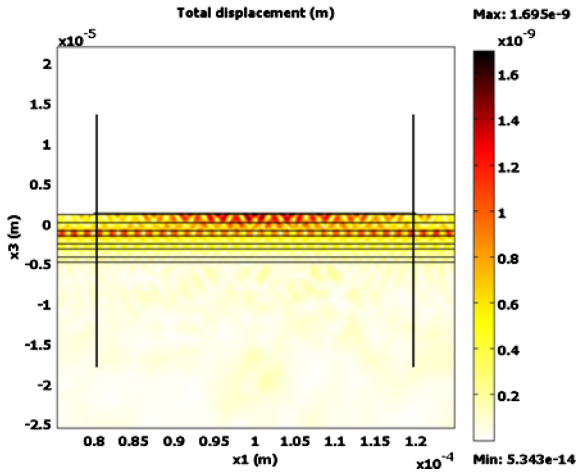

FIG. 4. (Color online) Particle displacement magnitude in staggered electrode configuration (solid vertical lines show edges of center top electrode in Fig. 2).

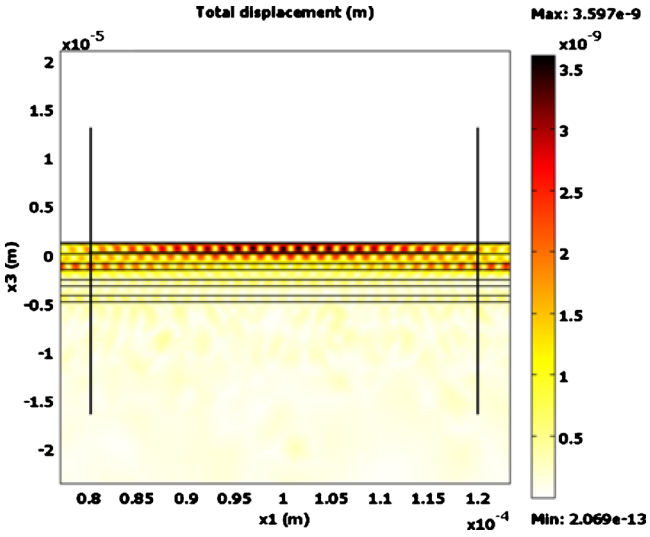

FIG. 5. (Color online) Particle displacement magnitude in electrode configuration with a floating top plate (solid vertical lines show edges of center buried electrode in Fig. 2).

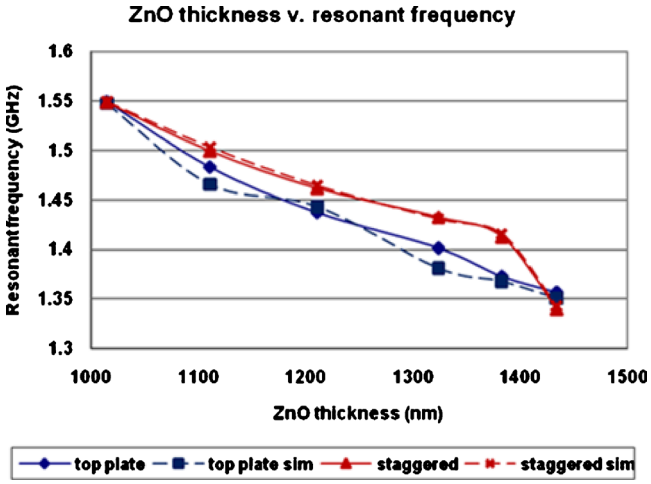

FIG. 6. (Color online) Measured and simulated resonant frequencies ("top plate" refers to the floating top plate configuration).

search for these modes in ZnO layers of varying thickness. The criteria for the desired mode structure are identical for each ZnO thickness. We simulate the devices structure for each of the ZnO thickness shown in Table I. Table II shows a comparison of the resulting simulated eigenfrequencies and effective velocities for this mode and the experimental results as the ZnO thickness varies. This data is also displayed graphically in Figs. 6 and 7. Expectedly, like the experimental data, the simulated frequency of the mode decreases with increasing ZnO thickness. Again like the experimental results, the effective velocity *increases* with increasing ZnO thickness. Notably, the simulation results agree with the experimental results within 1.5%. This high level of agreement is further confirmation that the observed mode is not pure but, in this case, is a coupled *hybrid* mode between the longitudinal and shear particle displacements in the ZnO. An interesting observation is that, for all ZnO thicknesses, the simulated staggered electrode configuration has a higher effective velocity than the floating plate configuration (confirming the energy trapping phenomenon) with exception to the thickest ZnO layer. Even this apparent anomaly as previously mentioned in Sec. II agrees with experiment within 0.24%.

TABLE II. Simulate and Measured resonant frequencies and effective velocities for varying ZnO thickness.

	Simulated and measured resonant frequencies (GHz) and effective velocities (m/s)									
	Floating top plate configuration					Staggered configuration				
ZnO	Simulated		Measured		Agreement	Simulated		Measured		Agreement
(nm)	GHz	m/s	GHz	m/s	(%)	GHz	m/s	GHz	m/s	(%)
1015	1.5476	3141	1.5496	3145	0.15	1.5497	3146	1.5482	3143	0.09
1111	1.4658	3257	1.4834	3296	1.18	1.5034	3341	1.4991	3331	0.29
1211	1.4430	3495	1.4374	3481	0.4	1.4645	3547	1.4614	3540	0.21
1324	1.3811	3657	1.4016	3711	1.46	1.4308	3789	1.4322	3792	0.1
1383	1.3678	3783	1.3731	3797	0.39	1.4153	3915	1.4123	3906	0.21
1434	1.3507	3873	1.357	3891	0.46	1.3430	3852	1.3398	3843	0.24

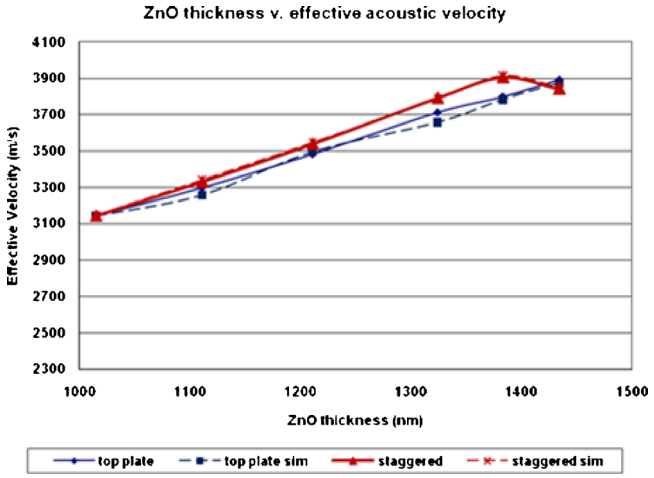

FIG. 7. (Color online) Measure and simulated effective velocities ("top plate" refers to the floating top plate configuration).

V. MODEL VALIDATION USING AN ALTERNATE STRUCTURE

Wathen *et al.*[15] observed what was deemed a *hybrid* mode with an effective velocity of 3500 m/s. The device structure used in that study is fundamentally different than the two used here in Sec. II and is shown schematically in Fig. 8. This structure is identical to that used by Corso *et al.*[3] Due to the assumed hybrid nature of the observed mode, we now simulate the exact device structure used in the 2009 study as a validation of the models presented in Secs. III and IV.

The COMSOL subdomains and boundary conditions are set up identically to those presented in Sec. IV. Dimensionally, the structure is identical to that used in Wathen *et al.*[15] An eigenfrequency simulation is used to find modes of a coupled nature in the ZnO layer and trapped under the electrodes.

With a 680 nm thick ZnO layer and 40 μm wide electrodes, the aspect ratio under the electrode is nearly 60:1. This extreme aspect ratio results in an extraordinary number of eigenfrequencies of the structure due to the number of possible spatial harmonics of the solutions. However, we find only one solution in the simulation that acceptably satisfies the conditions prescribed in Secs. III and IV. The simulated eigenfrequency of this mode was 2.594 GHz with the measured frequency in Wathen *et al.* equal to 2.588 GHz. The simulated effective velocity equaled 3527 m/s with the measured equal to 3519 m/s. The relative difference between the simulation and measurement, then, is equal to 0.2%. This alludes to a high confidence in the validity of the model presented in this study for describing the observed modes in the literature as a type of hybrid mode comprised of coupled longitudinal and shear particle displacements.

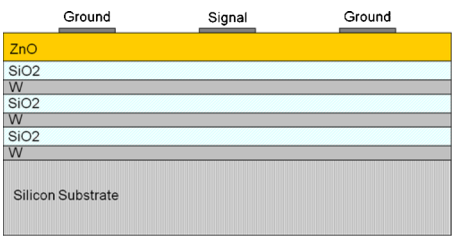

FIG. 8. (Color online) Typical LFE structure.

VI. CONCLUSIONS

Historically, there has been a large discrepancy between measured and theoretical velocities of the TSM in ZnO bulk acoustic resonators. We present an experimental verification of the discrepancy in ZnO SMR structures with two different electrode configurations. The ZnO thickness varied from 1015 to 1434 nm and the effective acoustic velocity through the thickness was found to increase with increasing ZnO thickness. A 2D theoretical analysis from the first principles of piezoelectric wave propagation is the presented. We show the possibility of the existence of a hybrid acoustic mode with coupled longitudinal and shear particle displacements. Finite element simulations of our experimental device structures show eigenmodes in the ZnO layer that satisfy the criteria of vertical and lateral energy trapping and a coupled mode structure. The eigenfrequency of the trapped mode at each thickness was used to calculate the effective velocity for that mode. These simulated velocities are within 1.46% of the experimentally measured velocities. We then validated the model by simulating a previously reported "hybrid" mode structure. The simulation results of this alternate device structure are within 0.2% of experimental measurements. We believe that this is a first step toward properly explaining the frequent discrepancy between measured and theoretical TSM values by way of a *hybrid* acoustic mode.

While already potential useful for electronic resonators, it is evident that with the proper surface chemical treatment, these devices are sufficient for sensing applications. However, with the coupled nature of the particle displacement, device performance is expected to degrade in a liquid sample as the longitudinal component is radiated into the fluid. With these results, it is expected that with further improvements on device structure and electrode configuration, the purity of the true TSM mode can be recovered and provide for more robust liquid-phase sensor.

ACKNOWLEDGMENTS

This work was supported in part by the V Foundation and by a SPORE grant in Head and Neck Cancer from the National Cancer Institute (No. 5 P50 CA128613–04). The authors also wish to thank Ryan Westafer for several helpful discussions regarding the finite element modeling.

[1]M.-A. Dubois and P. Muralt, Appl. Phys. Lett. **74**, 3032 (1999).
[2]S. L. Pinkett, W. D. Hunt, B. P. Barber, and P. L. Gammel, IEEE Trans. Ultrason. Eng. **49**, 1491 (2002).
[3]C. D. Corso, A. Dickherber, and W. D. Hunt, J. Appl. Phys. **101**, 054514 (2007).
[4]J. F. Rosenbaum, *Bulk Acoustic Wave Theory and Devices* (Artech House, Boston, 1988).
[5]L. Woo Wai, S. Yonghua, and K. Eun Sok, Proceedings of the 50th Frequency Control Symposium, 1996; Proceedings of the 1996 IEEE International, 1996, p. 258.
[6]G. Sauerbrey, Z. Phys. **155**, 206 (1959).
[7]W. D. Hunt, D. D. Stubbs, and L. Sang-Hun, Proc. IEEE **91**, 890 (2003).
[8]K. K. Kanazawa and J. G. Gordon, Anal. Chem. **57**, 1770 (1985).
[9]W. E. Newell, Proc. IEEE **53**, 575 (1965).

[10]J. de Klerk, Ultrasonics **8**, 159 (1970).
[11]J. S. Wang and K. M. Lakin, Appl. Phys. Lett. **42**, 352 (1983).
[12]M. Link, M. Schreiter, J. Weber, R. Primig, D. Pitzer, and R. Gabl, IEEE Trans. Ultrason. Eng. **53**, 492 (2006).
[13]W. Pang, H. Yu, J. W. Kwon, H. Zhang, and E. S. Kim, Proceedings of the Frequency Control Symposium and Exposition, 2004, p. 558.
[14]S. Wu, Z.-X. Lin, M.-S. Lee, and R. Ro, J. Appl. Phys. **102**, 084908 (2007).
[15]A. D. Wathen, F. Munir, and W. D. Hunt, Appl. Phys. Lett. **95**, 123509 (2009).
[16]W. Shockley, D. R. Curran, and D. J. Koneval, Proceedings of the 17th Annual Symposium on Frequency Control, 1963, Vol. 88, p. 88.
[17]COMSOL MULTIPHYSICS, MEMS Module Materials/Coefficients Library, 2008.